

In situ SAXS studies of the formation of sodium jarosite

Helen E. A. Brand,^{a,b,c*} Nicola V. Y. Scarlett,^c Ian E. Grey,^c Robert B. Knott^b and Nigel Kirby^a

^aAustralian Synchrotron, 800 Blackburn Road, Clayton, Victoria 3168, Australia, ^bANSTO, Locked Bag 2001, Kirrawee DC, New South Wales 2232, Australia, and ^cCSIRO Process Science and Engineering, Box 312, Clayton, Victoria 3168, Australia. E-mail: helen.brand@synchrotron.org.au

This paper reports the results of time-resolved synchrotron small-angle scattering and powder diffraction experiments where natrojarosites were synthesized *in situ* in order to observe the species produced at the earliest stages of nucleation. The sample temperatures were 333, 353 and 368 K. These compounds were synthesized by co-precipitation from solution on the Small and Wide Angle Scattering and Powder Diffraction beamlines at the Australian Synchrotron. Scattering data were collected continuously throughout the syntheses. The results presented here show that the first particles to form in solution appear to be amorphous and nucleate on the walls of the reaction vessel. Crucially, there is a single nucleation event which forms particles with an elliptical disc morphology which then grow uniformly before natrojarosite crystallization is observed in complementary powder diffraction data. This nucleation event may represent the key to controlling the growth of jarosites in industrial and environmental settings.

© 2013 International Union of Crystallography
Printed in Singapore – all rights reserved

Keywords: jarosite; *in situ*; SAXS.

1. Introduction

Jarosites [$A\text{Fe}_3(\text{SO}_4)_2(\text{OH})_6$, where A is typically K, Na or H_3O^+] and related minerals are of great interest to a range of mineral processing and research applications. In some industry settings jarosite formation is encouraged; for example, to aid the removal of iron species from solutions in electro-metallurgical smelting processes, the so-called ‘jarosite process’; however, in others, such as metal bioleaching applications, jarosite formation can hinder the process by creating a kinetic barrier, in the form of a passivation layer, to the desired reaction (Watling, 2006; Pradhan *et al.*, 2008; Dixon *et al.*, 2008). Also, jarosites are a major component of acidic soils and are present in significant amounts in acid mine drainage environments (Dutrizac & Jambor, 2000; Norlund *et al.*, 2010). Sustainable solutions to the jarosite stockpiles formed as the by-products of such industrial processes are being actively sought by companies engaged in such activities.

There has been a recent resurgence in interest in jarosite minerals since their detection on Mars by the MER rover Opportunity (Squyres *et al.*, 2004). In this context the presence of jarosite has been recognized as a likely indicator of water at the surface of Mars in the past and it is hoped that study of their formation mechanisms will provide insight into the environmental history of Mars (Madden *et al.*, 2004). Jarosites are also of considerable theoretical interest as model

compounds for spin frustration in Kagomé–Heisenberg anti-ferromagnetic materials (Wills, 2001; Grohol *et al.*, 2003). Therefore, knowledge of the formation mechanisms and stabilities of these minerals, with respect to the particles forming and their crystallinity, are indispensable prerequisites for understanding their potential environmental impacts. Moreover, any information regarding the nucleation and growth stages of these minerals is essential to controlling complex industrial processes where jarosite is formed.

To this end we are engaged in a program to study jarosites under a range of conditions. Here we report the results of *in situ* synchrotron small-angle X-ray scattering (SAXS) experiments designed to follow the nucleation and early growth phases of natrojarosite during the co-precipitation from solution. Previously the crystallization of micrometre-size particles of jarosite, as observed by synchrotron powder diffraction, was described in depth (Scarlett *et al.*, 2010; Grey *et al.*, 2011; Brand *et al.*, 2012).

The SAXS technique is extremely useful for the study of nanoscale particles. While diffraction gives information on the arrangement of atoms within a crystal lattice, SAXS returns information on the size, shape and surface condition of the bulk nanoparticles. Typically, SAXS provides information on particles in the size range of approximately 10–4000 Å.

SAXS is sensitive to variations in electron density in a system. Measurements are made of the isotropic scattering

intensity (I), as a function of the scattering vector, q . q is related to the scattering angle 2θ and λ is the X-ray wavelength according to equation (1),

$$q = 4\pi \sin \theta / \lambda. \quad (1)$$

The scattered intensity per unit volume is given by

$$I(q) = NV^2 \Delta\rho^2 P(q)S(q), \quad (2)$$

where N is the number of scattering particles per unit volume, V is their individual volume; $\Delta\rho$ is the scattering contrast between the particle and the surroundings, in this case, the solution; $P(q)$ is the form factor and $S(q)$ is the structure factor. In a dilute system such as this, the structure factor is effectively 1 and so the form factor will dominate the scattering pattern. A $\log I$ versus $\log q$ plot of the scattering data highlights the form factor and will typically exhibit power-law decays in intensity which are separated by exponential shoulders in the data. Analysis of SAXS patterns involves the fitting of model form factors to these features and physical properties are then extracted from the model. Shoulders in the data indicate the presence of a characteristic dimension in the system of interest (Panzarella *et al.*, 2007). The choice of model when fitting SAXS patterns is crucial and highly dependent on the system being studied.

With the advent of bright synchrotron sources, rapid time-resolved studies of the formation of particles can be followed using SAXS. A variety of minerals have been studied in this way include zeolites (Panzarella *et al.*, 2007), calcium carbonates (Pontoni *et al.*, 2003), aluminium hydroxide (Li *et al.*, 2008) and nanoparticulate silica (Fouilloux *et al.*, 2010). To date there have been no SAXS studies of jarosite minerals, *in situ* or *ex situ*, except for our initial reports of this study (Brand *et al.*, 2012).

2. Experimental method

Jarosite forms readily by co-precipitation on warming a solution containing ferric and alkali sulfates. This study was focused on sodium jarosites. Here, 1.74 g of $\text{Fe}_2(\text{SO}_4)_3 \cdot x\text{H}_2\text{O}$ and 0.57 g of Na_2SO_4 were dissolved in 10 ml of deionized water and filtered through a Millipore filter (0.22 μm) to remove any nuclei. Portions of each solution were transferred to 1.0 mm quartz capillaries for synchrotron SAXS experiments. The capillaries were mounted in a custom-made Swagelok pressure stage and pressurized using nitrogen gas at 40 kPa to prevent boiling of the solution upon heating. Heat was applied *via* a hot-air blower placed directly under the capillary and the temperature monitored and controlled *via* a thermocouple. The reaction vessel was oscillated about its axis during data collection to ensure (i) uniform heating and (ii) constant stirring of the solution. The experimental set-up is described in greater detail elsewhere (Scarlett *et al.*, 2008). Experiments were conducted on the SAXS/WAXS beamline at the Australian Synchrotron (Fig. 1) at sample temperatures of 333, 353 and 368 K. The lowest temperature represents the upper limit of realistic bio-heap temperature conditions (Watling, 2006). The beamline set-up was as follows: a 7 m

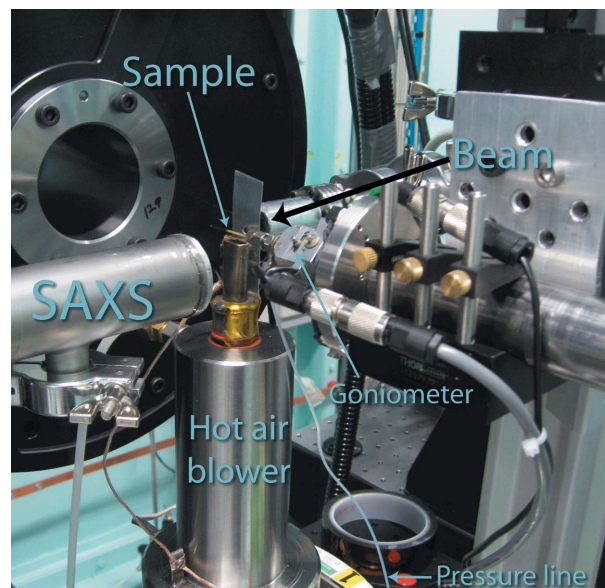


Figure 1
Experimental set-up in place on the SAXS/WAXS beamline at the Australian Synchrotron.

SAXS camera was used at a wavelength of 1.2398 \AA , to give a calibrated SAXS q -range of 0.00179–0.13182 \AA^{-1} and a wide-angle X-ray scattering (WAXS) 2θ range of 10–30°. While the WAXS data were recorded, they were not intended to be used for detailed analysis. We have already carried out much higher resolution complementary powder diffraction measurements on the powder diffraction beamline at the Australian Synchrotron. The WAXS data are intended to provide a check that the reactions are progressing in a similar manner to the powder diffraction experiments and to follow the phases produced. Thus any 'PD' data referred to here comes from the companion study described by Scarlett *et al.* (2010), Grey *et al.* (2011) and Brand *et al.* (2012).

SAXS/WAXS data were collected contiguously throughout the reactions as jarosite formed within the capillary reaction vessels. Initial room-temperature solution datasets were recorded before the temperature was increased. At the outset, 5 s datasets were collected contiguously. At 368 K all datasets were collected in this way while at the lower temperatures, after an initial period of contiguous data acquisition, the acquisition rate was slowed to a 5 s dataset collected once a minute for the remainder of the experiment. At 353 K this change in acquisition rate occurred after 2 h, and at 333 K after ~ 2.5 h. Experiment durations were taken from the companion PD experiments. They were stopped when peak growth was no longer visible in the PD data. For 368 K this was after 2 h, at 353 K this was after 4 h, and at 333 K this was after 11 h.

3. Results

Initial room-temperature SAXS patterns did not show any pre-existing particles in any of the starting solutions. Upon heating of the capillaries, particle formation in the solutions

proceeded rapidly with the particles adhering to the walls of the capillary. Simultaneous WAXS and complementary powder diffraction experiments (Brand *et al.*, 2012) show that jarosite was the only material to crystallize during the experiments.

3.1. Optical microscopy

Several days following the SAXS experiments, capillaries from each of the temperature syntheses were examined using an optical microscope. The crystals, identified from the accompanying PD and confirmed in the WAXS datasets as sodium jarosite, are well formed and clearly visible in the capillaries. Fig. 2 shows optical microscope images of the material formed at each temperature, for temperatures of (a) 333 K, (b) 353 K and (c) 368 K; all are on the same length scale. The quality of the images is limited as the images were taken through the capillary wall and solution to preserve the solution equilibrium within. At all temperatures the crystals were reasonably well dispersed along the wall and extended well outside the region exposed to the intense X-ray beam. Slight aggregation was apparent in the image taken at 368 K. The crystals were homogeneously sized at all temperatures and formed a layer on the walls of the capillaries. At 368 K they had an average size of $\sim 2 \mu\text{m}$, while the crystals grown at 353 K were larger, with an average size of $\sim 4 \mu\text{m}$. The small size of the 368 K crystals compared with the 353 K crystals is possibly a consequence of a larger number of initial nuclei forming at the higher temperature, the growth of which is then limited by the space available; however, there is considerable uncertainty since the reaction times were very different for the two temperatures. The 333 K crystals were significantly smaller than at the higher temperatures, much less than $1 \mu\text{m}$ in size. At 353 and 368 K the crystals appeared to be well formed, sub-euhedral in habit with a polyhedral appearance. Fairchild (1933) reports rhombohedral crystals, which is consistent with the crystal habit observed here. The crystals were pleochroic. However, effects from the capillary and solution make it difficult to distinguish the degree of pleochroism (*i.e.* whether the crystals are di- or tri-chroic), thus no insight as to their symmetry can be gained this way. It should also be noted that these images were taken several days after the SAXS experiments and so do not represent the jarosite during the experiments, but rather an end point of the synthesis.

3.2. SAXS

Raw two-dimensional SAXS datasets were displayed and reduced using *Saxs15ID* software (Cookson *et al.*, 2006). Patterns were normalized to the beamstop intensity before an initial room-temperature pattern was subtracted from each subsequent pattern. This subtraction removed scattering from the starting solution and capillary, and was essential, especially early in the reaction when there are only a few small particles present. Room-temperature (rather than at the reaction temperature) patterns were subtracted to ensure that no particle information was lost due to the speed at which the

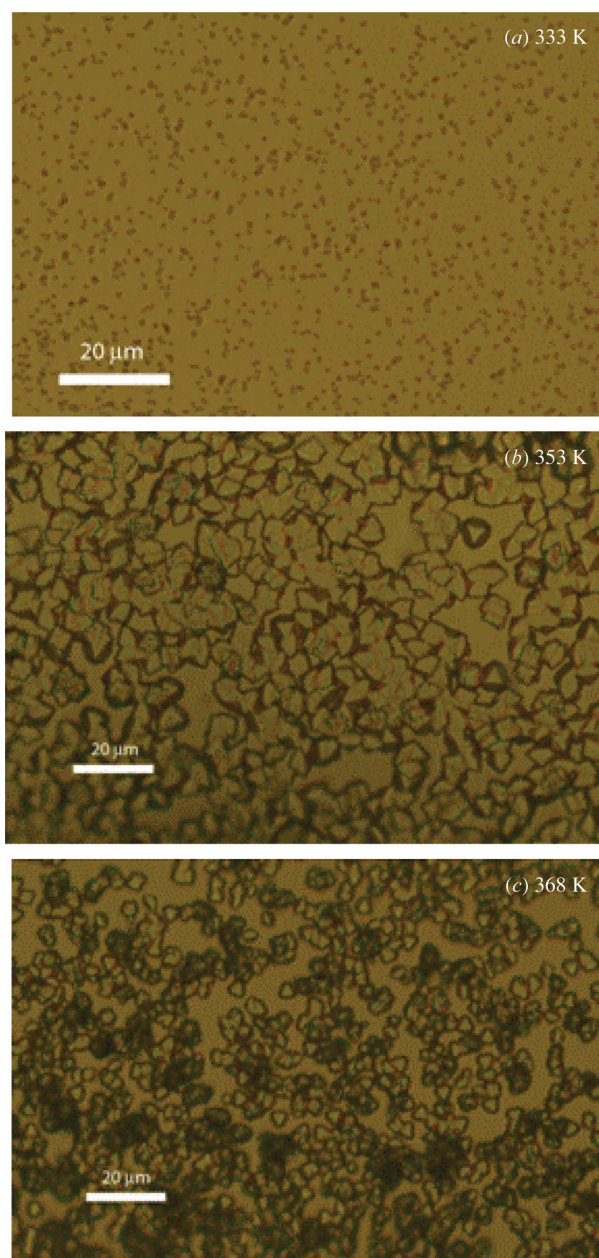


Figure 2
Optical microscope images taken after the experiments showing the crystals formed in the capillaries at each temperature.

reaction progresses once heating commences. The two-dimensional normalized and subtracted SAXS patterns were reduced to one-dimensional profiles. Fig. 3 shows a three-dimensional representation of the time sequence of the normalized and subtracted SAXS profiles where the x -axis is the q -scale, the y -axis is intensity and z is the dataset number (time). The plot is absolute scaled with respect to water. The plot clearly shows the appearance and development of the particles as the reaction progresses.

A selected time sequence for sodium jarosite formation at 368 K is presented in Fig. 4. At all times where particle scattering is apparent there appears to be a sharp interface

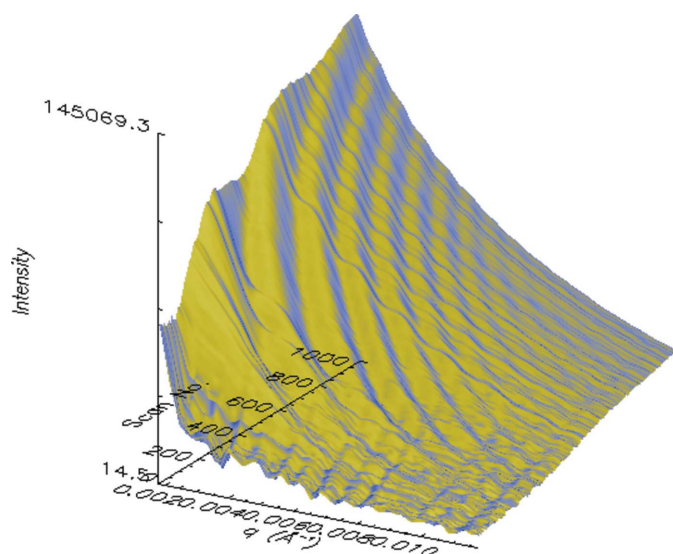


Figure 3
A sequence of SAXS patterns from the formation of jarosite at 368 K. The data are represented in a three-dimensional plot with q along the x -axis, scan number (time) on the y -axis and intensity along the z -axis.

between the solution and the particles. Fig. 4 shows the growth of the particles. There are three distinct SAXS morphologies (denoted here as ‘Guinier’, ‘Fringed’ and ‘Porod’ regions) apparent in the data. Although there are three morphological regions, the data show the evolution of a smooth function through the experiment. Table 1 details the reaction times that each morphological regime was observed at each of the synthesis temperatures. The scattering from the earliest particles visible in the data has a simple Guinier form; at 368 K this is the portion of the reaction between 2 and 3 min. As the particles grow, more detail about their shape and dimensions emerges and the patterns begin to display ‘fringes’, which move down in q -value with time. Eventually, at 353 and 368 K,

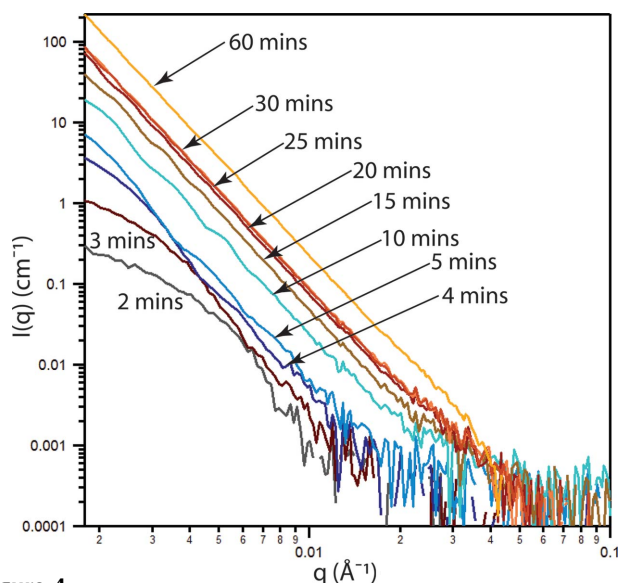


Figure 4
A sequence of reduced SAXS patterns from the formation of jarosite at 368 K. The data are represented in a two-dimensional plot with q along the x -axis and intensity along the y -axis.

Table 1

Timescales for each SAXS pattern morphology at each reaction temperature.

| | Temperature (K) | | |
|----------------|-----------------|------------|-----------|
| | 333 | 353 | 368 |
| Guinier region | 160–260 min | 9–13 min | 0–3 min |
| Fringed region | 360–690 min | 13–70 min | 3–20 min |
| Porod region | N/A | 70–660 min | 20–74 min |

all of the dimensions of the particles are too large to be directly resolved on this SAXS scale and the profiles are dominated by Porod scattering. At 333 K, allocated beam-time constraints meant that the reaction had to be terminated before the particles had grown. It is assumed that this reaction would proceed in similar fashion to those at higher temperature; however, there is no information from the corresponding Porod region for this temperature.

Also evident in Table 1 is an induction period before particles are visible in the SAXS data which decreases with increasing temperature. During this initial period the amount of material may be below detection limits in terms of both particle size and concentration. It is worth noting that this induction period is not the same as for the companion experiments on the powder diffraction beamline. The induction periods for SAXS and PD refer to different quantities. In SAXS it refers to the initial appearance of particles of sufficiently different scattering contrast to the solution of sufficient size and concentration to be observed. In powder diffraction it refers to the time at which crystals of adequate size and with sufficient long-range order to be observed initially appear. Significantly different induction periods were observed for the parallel SAXS and PD experiments. For the SAXS experiments, the values were 160, 9 and 0 min at 333, 353 and 368 K, respectively. For the PD experiments, the induction times were 19 and 9 min at 353 and 368 K, respectively. The fact that the SAXS induction periods were consistently shorter than those for PD may mean that the first particles observed were too few, too small or insufficiently ordered to be detected by PD. Insufficient ordering, *i.e.* the particles are amorphous, is most likely. The sensitivity of the PD detector and the WAXS detector on the SAXS beamline were tested using solutions of jarosite in water at known concentrations. For the PD beamline, the detection limit was between 0.25 and 0.5 wt%, while, for the WAXS detector on the SAXS beamline, measureable peaks were still visible for a 0.25 wt% solution.

The monodispersity of the particles observed by SAXS, combined with the optical images from final products of SAXS and equivalent PD experiments, suggests that the particles nucleated in adequate numbers to be observed by diffraction if they were of sufficient long-range order. The size of the particles calculated from the SAXS data (up to ~ 3500 Å) is also well above the limits of crystallite size observable by PD. This suggests that the initial particles observed in the SAXS data lacked adequate long-range order to be observed by diffraction. This is illustrated in Fig. 5 which shows the scattering curves ten minutes into the 353 K synthesis for (a) SAXS and (b) the parallel powder diffraction experiment.

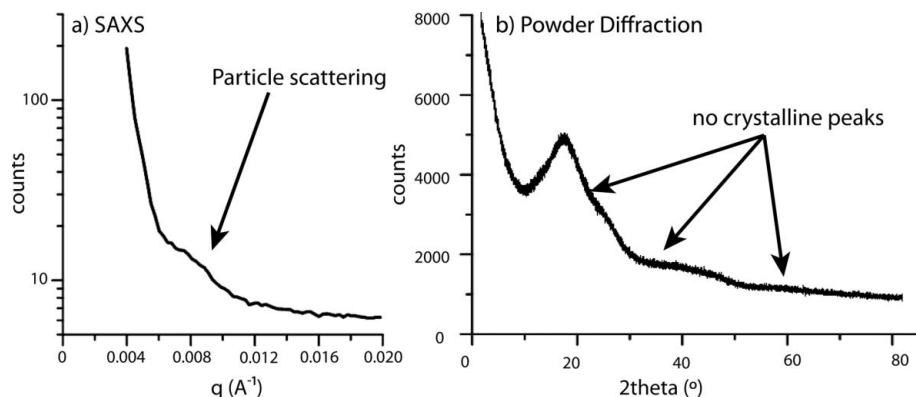


Figure 5 Scattering patterns ten minutes into the 353 K synthesis for (a) SAXS and (b) the parallel powder diffraction experiment.

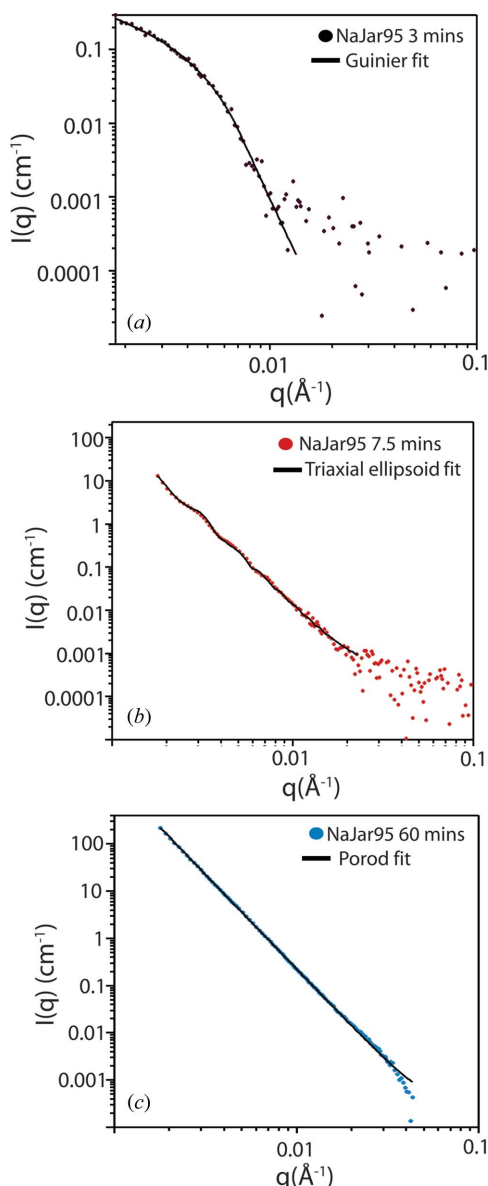


Figure 6 Typical patterns for each of the morphological regions in the SAXS data. The coloured data points are the SAXS observations and the solid line is the model fit.

There is clearly no observable crystalline material in the diffraction pattern; the broad peaks in the background are an amorphous scattering contribution from the capillary and solution.

The following sections describe each of the morphological regions present in the SAXS data and the information obtained from each. Fig. 6 shows a typical fit to a pattern from each of the regions (at 368 K): (a) from the Guinier region, (b) from the fringed region and (c) from the Porod region.

In the first two morphological regions, the so-called ‘Guinier’ and ‘fringed’ regions, it is possible to make an assessment of the size of the particles

evident in the SAXS profiles. In the fringed region it is also possible to infer something about the shape of the particles. In the third, the Porod, region, the particles are too big to determine size information but we can gain some insight to the surface of these particles.

The first SAXS profiles where particles are visible have a simple Guinier form. The particles appear quite abruptly from the background over the course of a very short time, only a few tens of seconds, even at the lowest temperature. The profiles were fitted with a Guinier relation [equation (3) where $I(q)$ is the observed intensity, ρ_0 is the particle scattering length density, V the volume and R_g the radius of gyration]. For a simple sphere the radius of gyration is related to the radius of the particle, R , by the expression $R^2 = (3/5)R_g^2$,

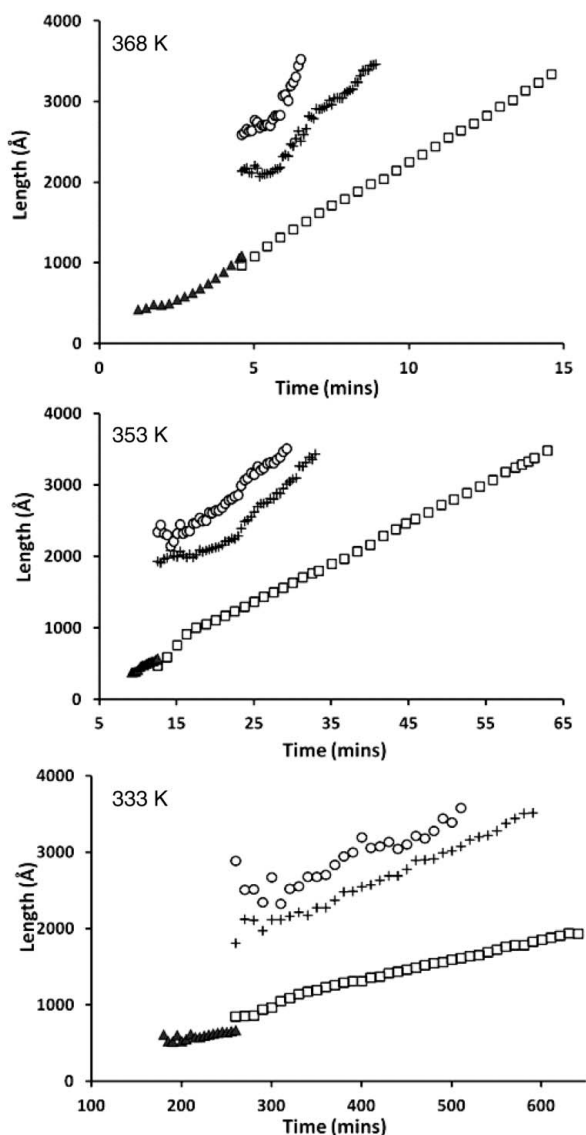
$$I(q) \cong \rho_0^2 V^2 \exp(-q^2 R_g^2/3). \quad (3)$$

The smallest objects observed at any of the temperatures are $\sim 300 \text{ \AA}$ in radius. Objects smaller than this still fall well inside the q -range measured; however, in the initial stages of the synthesis, when there are very few very small particles, they are indistinguishable from the background.

Fig. 7 shows the size variation with time at each of the three temperatures for the Guinier region and the fringed region. The profiles in which particles were observed to show a fringed morphology were fitted using the NIST SANS models (Kline, 2006). The best fit to the data was found to be a triaxial ellipsoid with an elliptical disc form and low eccentricity (almost circular cross section).

The triaxial ellipsoid form factor model assumes, using conventional nomenclature for the semi-major axes of a generic triaxial ellipsoid, that, if $a \leq b \leq c$, then the form factor $P(q)$ of the triaxial ellipsoid may be written as (Feigin & Svergun, 1987)

$$P(q) = \frac{\text{scale}}{V_{\text{el}}} \int_0^1 \int_0^1 \varphi^2 \left\{ q \left[a^2 \cos^2(\pi x/2) + b \sin^2(\pi x/2)(1 - y^2) + c^2 y^2 \right]^{1/2} \right\} dx dy, \quad (4)$$


Figure 7

Variation in size of particles over the Guinier and fringed regions at each temperature. For each temperature the Guinier data are represented by a filled triangle, the elliptical a -axis by an open square, the elliptical b -axis by a cross, and the elliptical c -axis by an open circle. All data have been plotted only while the axial-length values remain within the available SAXS q -scale. For clarity not all data points are included: at 333 K, in the Guinier region, data are plotted every 5 min, and in the fringed region, every 10 min; at 353 K, all datasets are present except for the elliptical a -axis within the fringed region, where datasets are presented every 1.5 min; at 368 K, in the Guinier region, data are presented every 0.25 min, while in the fringed region the elliptical a -axis is presented every 0.5 min, and all data are shown for the other axes. Fitting errors are comparable with the size of the data point.

where ‘scale’ is a parameter relating to the amount of material (similar to the Rietveld scale factor), V_{e1} is the volume of the ellipsoid and the function $\varphi^2(x)$ is defined as

$$\varphi^2(x) = 9 \left(\frac{\sin x - x \cos x}{x^3} \right)^2. \quad (5)$$

This model of a particle with an elliptical disc-shaped SAXS envelope agrees with the optical microscopy observations of

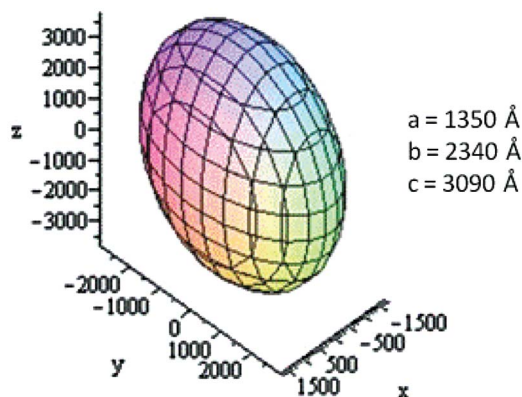
particles commonly with triangular faces that form on the walls of the capillary and it is reassuring that at each temperature the value of the smallest ellipsoid axis agrees well with the largest sizes obtained from the Guinier region fits. [For an elliptical particle, R_g is given by: $R_g^2 = (1/5)(a^2 + b^2 + c^2)$.]

The SAXS profiles at all temperatures reveal a narrow size distribution (low polydispersity) within the particle populations. Parameters in the model are: scale, a , b , c (the axes of the ellipse), the scattering length density of the particle, the scattering length density of the solution and the background. In this case the scattering contrast between the particle and solution was not refined as this could have introduced bias towards the solution through its predominance which could have resulted in unrealistic fitting, especially at the beginning of the reaction when there is very little particulate material. These were fixed at values calculated for Na-jarosite and water for the ellipsoid and solution, respectively.

Fig. 8 shows a three-dimensional representation of the particle shape; in this case, after 5 min in the 368 K synthesis. As will be discussed in more detail below, there is little difference between the axial ratios calculated for the different temperatures.

The largest dimension that can be determined on this q -scale is ~ 3500 Å. As such, elliptical axes lengths which are larger than this in the model fitting are not as consistent and once an axis has reached this limit the fitted values associated with it have not been included in the figure. However, fitting of all axes continued while the smaller axes continue to refine reasonably and within limits. The fitting errors associated with the lengths of the axes are similar for each axis and temperature, and of the order of tens of angstroms which is comparable with the size of the data point in the figure whilst the axis in question is within scale. However, once the axis has moved out of the available size range then the error increases, as might be expected, to be of the order of 200 Å.

All three elliptical axes grow at a steady rate throughout the period where they are visible at each temperature. The b - and c -axes grow at a slightly quicker rate than the a -axis, and at


Figure 8

Example of the modelled shape of the particles indicated from SAXS fits to the fringed section of the data, in this case from the 368 K data after 5 min.

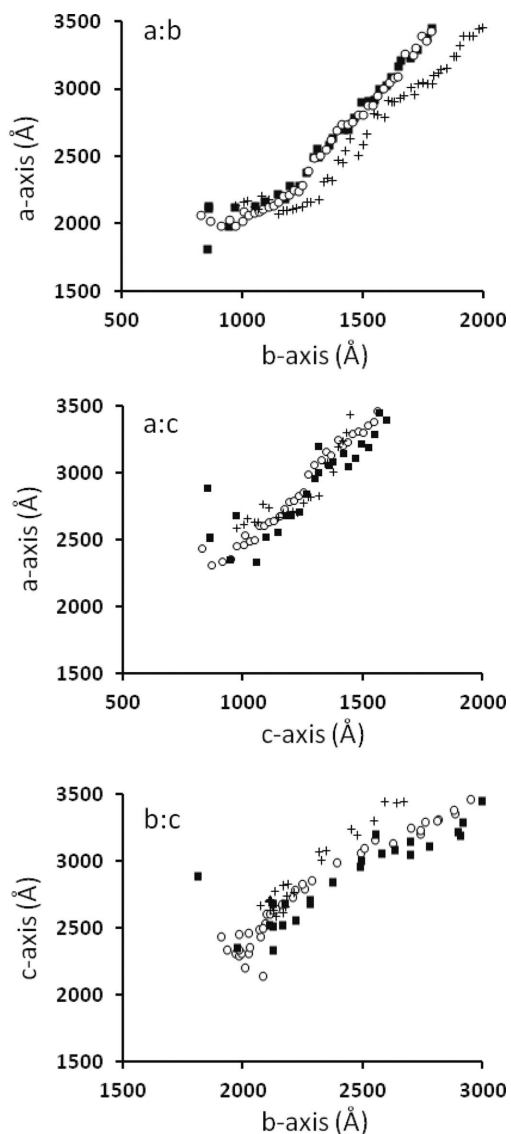


Figure 9
Axial ratios of the particles in the fringed region. In each plot the closed squares are the 333 K data, open circles are the 353 K data, and the crosses are the 368 K data.

very similar rates to each other. Plots of the ratios of the elliptical axes lengths, Fig. 9, confirm this and show that at each temperature the particles follow a similar size–shape growth path, with no significant anisotropy apparent. Towards the end of the section of the reaction where fringed patterns are observed, there is a suggestion of an increase in polydispersity as the oscillations in the scattering curve become less pronounced and the fit begins to deteriorate at values of high q .

Fig. 10 shows the volume growth (left-hand panels) and number density (right-hand panels) of the particles during the fringed region of the synthesis at each temperature while the axes remain within observable scale. All temperature syntheses show similar volume growth patterns, with a change in the speed of growth evident about halfway through the fringed region at 353 K. This suggests a change in mechanism in these early stages of growth but requires a more stringent kinetic

study than these data support to investigate further. Needless to say, they are not coincident with the later growth mechanism changes seen in our PD data (Scarlett *et al.*, 2013). The number density increases with time at each temperature. Final number densities have been calculated for the final patterns where the axes are in range at each temperature; at 333 K, a value of 1.60×10^6 is returned; at 353 K, N is 4.02×10^6 ; and at 368 K, 1.31×10^7 ; unfortunately, these cannot be verified by extraction and measuring of the jarosites as this would break the equilibrium within the capillary and the jarosite would decompose. Deviations from a smooth increase in the number density at 353 K correlate with small fluctuations from the overall trend in the volume growth and are likely a correlation between these two fit parameters.

Once the particles have grown to a size which is too large to be fitted with the elliptical model on the available q -scale, the profiles take on a Porod form (*e.g.* Fig. 6c); accordingly, these profiles (at 353 and 368 K) have been fitted with a simple power-law equation,

$$I(q) = Bq^{-P} + \text{Bkgd.} \quad (6)$$

The value of P in this equation is indicative of the condition of the surface of the particle and B gives a relative measure of the amount of material present. In these experiments, at all temperatures and times, P has a value close to 4, which represents scattering from a smooth surface. As the formation proceeds there is a small, but noticeable, decrease in the fitted value of P from 4.0 to ~ 3.8 at each temperature, which may represent the development of crystal faces on a previously uniform surface as the particles crystallize. This broadly correlates with the commencement of natrojarosite crystallization observed in the companion higher-resolution powder diffraction measurements as well as the simultaneous WAXS measurements.

4. Discussion

The SAXS data from these *in situ* jarosite syntheses have given us important insights into the early stages of the formation of natrojarosite. As with the potassium jarosites described by Brand *et al.* (2012), at all stages of the SAXS experiment where particles are evident there is only evidence for one particle population. This suggests that under these preparative conditions there is a single nucleation event. Observations of particle size and numbers by optical microscopy after the experiments, together with the assumption of a single nucleation event, suggests that it is the number of particles which nucleate, rather than their rate of growth, which is temperature dependent. At higher temperatures, more nuclei form, but these quickly become restricted by their surrounding neighbours. This results in more moderately sized crystals at high temperature and fewer crystals at lowest temperature.

A single nucleation event is expected if, as has been suggested by others (*e.g.* Grey *et al.*, 2011), jarosite formation/nucleation requires very specific conditions, particularly with regard to pH. At higher temperatures these favourable

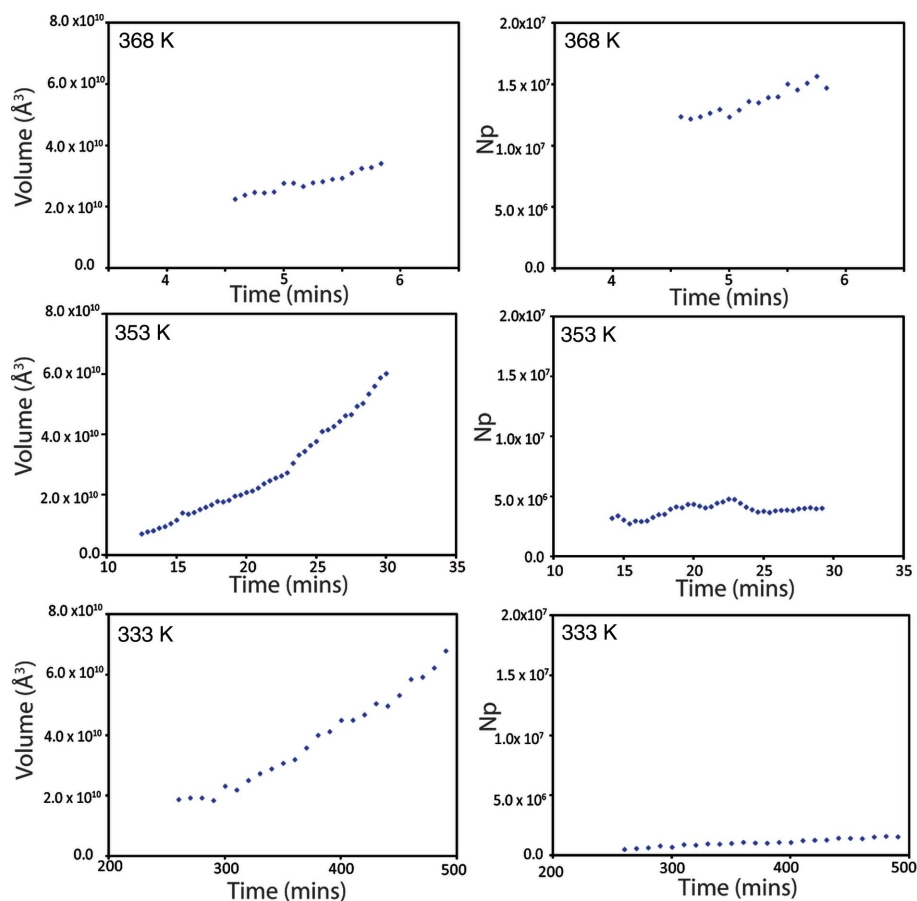


Figure 10
Variation in the volume (left-hand panels) and number density (right-hand panels) of the particles over the fringed region at each temperature. For each temperature, data have been plotted only while the axial-length values remain within the available SAXS q -scale. For clarity, not all data points are included: at 333 K, the data are plotted every 10 min; at 353 K, data are plotted every 0.4 min; at 368 K, all data are shown. Fitting errors are comparable with the size of the data point.

conditions only persist for a very limited portion of the reaction. Thus, controlling the nucleation event may be the key to preventing the formation of jarosite in industrial applications.

Unfortunately the SAXS data are not suitable for the extensive kinetic analysis which has already been applied to the powder diffraction data (Brand *et al.*, 2012; Scarlett *et al.*, 2013). As such, there will only be a qualitative discussion of the kinetics here. The growth rate of the three elliptical dimensions is comparable (see Fig. 7) at each temperature. With a temperature rise, the rate increases, as would be expected. This is especially apparent by looking qualitatively at the relative change in growth rate between 353 and 368 K where there is a large change for a moderately small energy input compared with that between 333 and 353 K.

It is apparent from the difference in the induction times observed in the SAXS and PD experiments (Fig. 5) that the particles apparent in the SAXS data are not initially crystalline, and are not crystalline for a considerable part of the synthesis; diffraction peaks are not evident in the data (WAXS and high-resolution PD) until much later, *e.g.* ~30 min, at 368 K. It is possible that these particles are crystalline but that the crystallite size, the size of the diffracting domain, is too small to give diffraction peaks. However, we cannot determine

this from these measurements. To the techniques employed here, these early particles simply appear amorphous. Given the sensitivity of the available detectors at SAXS/WAXS and PD, it is reasonable to assume that if crystalline peaks are not from these *in situ* experiments then at that point in the synthesis the material is amorphous.

With this in mind it is possible that these early amorphous particles are not jarosite but are precursor phases; in a concentrated Fe³⁺ environment a dimer linked by hydroxyl bridges may be formed (Dutrizac, 1979): $2\text{Fe}^{3+} + 2\text{H}_2\text{O} \rightarrow \text{Fe}_2(\text{OH})_2^{4+} + 2\text{H}^+$. Such species may also contain sulfate, bisulphate or sulfate–bisulphate ligands and can develop to form polymeric structures. These small polymer chains may be considered as distorted edge-shared Fe³⁺ octahedra. It is unlikely that jarosite could be distinguished from these polymer chains by including scattering length densities (SLDs) in the elliptical disc model fits as there is only $0.1 \times 10^{-5} \text{ \AA}^{-2}$ difference in their calculated SLDs. There is no evidence of chain-like structures in the SAXS patterns, and such dimers would be much smaller than the particles observed in the SAXS data. However, the ellipsoid particles observed could be aggregations of such structures (Margulis *et al.*, 1976;

Dutrizac, 1979). Recent *ex situ* studies (Grey *et al.*, 2013) have shown that in the potassium jarosite system this precursor phase is Maus salt, $\text{K}_5\text{Fe}_3\text{O}(\text{SO}_4)_6 \cdot 10\text{H}_2\text{O}$.

5. Summary

Combined *in situ* diffraction and SAXS experiments have demonstrated the power of *in situ* measurements to investigate the formation of complex systems such as natrojarosite. A single nucleation event, observed by SAXS, is followed by the uniform growth of elliptical amorphous particles. These particles are initially smooth-surfaced, but, in the later stages of the reaction, surface modification begins. This modification of the surfaces, towards a more fractal surface, is coincident with the onset of crystallization from the powder diffraction measurements.

It seems evident that the next stage in these studies should be to investigate these important precursor phases to find out if they are truly amorphous or colloidal agglomerations or, indeed, agglomerations of very fine crystallites. This may have profound implications for the methods subsequently employed to promote or prohibit their growth. Whatever their composition, it seems clear that for those who wish to hasten

the formation of jarosite, e.g. in Zn processing solutions, controlling first the nucleation through rationalization of the conditions to enhance nucleation and then promote the growth of these precursor phases will be key.

This research was undertaken on the Small and Wide Angle Scattering and Powder Diffraction beamlines at the Australian Synchrotron, Victoria, Australia, with assistance from Kia Wallwork, Adrian Hawley and Stephen Mudie. We acknowledge travel funding provided by the merit domestic travel fund managed by the Australian Synchrotron. Thanks are extended to Matthew Rowles, Ian Madsen, Miao Chen and Mark Styles for help with the syntheses and synchrotron data collections.

References

- Brand, H. E. A., Scarlett, N. V. Y. & Grey, I. E. (2012). *J. Appl. Cryst.* **45**, 535–545.
- Cookson, D., Kirby, N., Knott, R., Lee, M. & Schultz, D. (2006). *J. Synchrotron Rad.* **13**, 440–444.
- Dixon, D. G., Mayne, D. D. & Baxter, K. G. (2008). *Can. Metall. Q.* **47**, 327–336.
- Dutrizac, J. E. (1979). *The Physical Chemistry of Iron Precipitation in the Zinc Industry, Lead-Zinc-Tin '80*, edited by J. M. Cigan, T. S. Mackey & T. J. O'Keefe, pp. 532–564. Warrendale: TMS-AIME.
- Dutrizac, J. E. & Jambor, J. L. (2000). *Rev. Min. Geochem.* **40**, 405–452.
- Fairchild, J. G. (1933). *Am. Mineral.* **18**, 543–547.
- Feigin, L. A. & Svergun, D. I. (1987). *Structure Analysis by Small Angle X-ray and Neutron Scattering*. New York: Plenum Press.
- Fouilloux, S., Désert, A., Taché, O., Spalla, O., Daillant, J. & Thill, A. (2010). *J. Colloid Interface Sci.* **346**, 79–86.
- Grey, I. E., Scarlett, N. V. Y., Bordet, P. & Brand, H. E. A. (2011). *Mineral. Mag.* **75**, 2775–2791.
- Grey, I. E., Scarlett, N. V. Y. & Brand, H. E. A. (2013). *Mineral. Mag.* **77**, 29–268.
- Grohol, D., Huang, Q., Toby, B., Lynn, J., Lee, Y. & Nocera, D. (2003). *Phys. Rev. B.* **68**, 094404.
- Kline, S. R. (2006). *J. Appl. Cryst.* **39**, 895–900.
- Li, J., Cookson, D. J. & Gerson, A. R. (2008). *Cryst. Growth Des.* **8**, 1730–1733.
- Madden, M. E., Bodnar, R. J. & Rimstidt, J. D. (2004). *Nature (London)*, **431**, 821–823.
- Margulis, E. V., Getskin, L. S., Zapuskalova, N. A. & Beisekeeva, L. I. (1976). *Russ. J. Inorg. Chem.* **21**, 996–999.
- Norlund, K. L., Baron, C. & Warren, L. A. (2010). *Chem. Geol.* **275**, 235–242.
- Panzarella, B., Tompsett, G., Conner, W. C. & Jones, K. (2007). *Chem. Phys. Chem.* **8**, 357–369.
- Pontoni, D., Bolze, J., Dingenouts, N., Narayanan, T. & Ballauff, M. (2003). *J. Phys. Chem. B*, **107**, 5123–5125.
- Pradhan, N., Nathsarma, K. C., Srinivasa Rao, K., Sukla, L. B. & Mishra, B. K. (2008). *Miner. Eng.* **21**, 355–365.
- Scarlett, N. V. Y., Grey, I. E. & Brand, H. E. A. (2010). *Am. Mineral.* **95**, 1590–1593.
- Scarlett, N. V. Y., Grey, I. E. & Brand, H. E. A. (2013). *J. Synchrotron Rad.* **20**, 366–375.
- Scarlett, N. V. Y., Madsen, I. C. & Whittington, B. I. (2008). *J. Appl. Cryst.* **41**, 572–583.
- Squyres, S. W., Arvidson, R. E., Bell, J. F., Brückner, J., Cabrol, N. A., Calvin, W., Carr, M. H., Christensen, P. R., Clark, B. C., Crumpler, L., Marais, D. J., d'Uston, C., Economou, T., Farmer, J., Farrand, W., Folkner, W., Golombek, M., Gorevan, S., Grant, J. A., Greeley, R., Grotzinger, J., Haskin, L., Herkenhoff, K. E., Hviid, S., Johnson, J., Klingelhöfer, G., Knoll, A. H., Landis, G., Lemmon, M., Li, R., Madsen, M. B., Malin, M. C., McLennan, S. M., McSween, H. Y., Ming, D. W., Moersch, J., Morris, R. V., Parker, T., Rice, J. W., Richter, L., Rieder, R., Sims, M., Smith, M., Smith, P., Soderblom, L. A., Sullivan, R., Wänke, H., Wdowiak, T., Wolff, M. & Yen, A. (2004). *Science*, **306**, 1698–1703.
- Watling, H. (2006). *Hydrometallurgy*, **84**, 81–108.
- Wills, A. S. (2001). *Phys. Rev. B*, **63**, 064430.